Detection of Human Breathing in Non-Line-of-Sight Region by Using mmWave FMCW Radar

Gen Li, Yun Ge, Yiyu Wang, Qingwu Chen, and Gang Wang, *Member, IEEE*

***Abstract*— Detection of an actionless human hidden in the non-line-of-sight (NLOS) region can be implemented by combining NLOS object detection and vital sign detection. Since the radar waves suffer from severe multipath effects in NLOS environment, a specific detection scheme is required for human position estimation and breathing detection with 77-GHz frequency-modulated continuous-wave (FMCW) radar. After radar surveying of the NLOS environment, local coordinates and the radar wave reflection and propagation model can be established on-site. An NLOS target positioning algorithm, referred to as the NLOS multipath target searching and position estimating (NLOS-mTSPE) algorithm, is proposed to recognize the typical wave propagation paths in the NLOS area for accurate positioning of the human in the NLOS region. According to the recognized signal path, human breathing signals can be correctly extracted and the breathing rate can be acquired with an average error of 1%. The proposed scheme is demonstrated by the detection in a corridor behind an L-shaped corner, in which both the accurate human position and breathing rate can be acquired. The maximum detectable distance and the maximum localizable distance in the NLOS region are analyzed.**

***Index Terms*— Breathing signals, corner, FMCW radar, NLOS, position estimation.**

I. Introduction

RADAR detection of a target in the non-line-of-sight (NLOS) region has found many important applications in both civil and military actions. For certain application scenarios, it is required to determine whether a target in the NLOS region is a human. For instance, in fire rescue/earthquake relief, it is desired to find alive people trapped behind the corner. In military action, it is required to confirm whether or not there are enemies hiding behind corners. When the person in the NLOS region stays actionless, the radar usually recognizes it as an object target. If additional vital signs can be detected from such a target, the stock-still target can be determined as a person. Therefore, the detection of the actionless human hidden in the NLOS region can be implemented by combining NLOS object detection and vital sign detection.

Manuscript received 4 May 2022; revised 17 July 2022; accepted 6 September 2022. Date of publication 21 September 2022; date of current version 5 October 2022. This work was supported in part by the University Synergy Innovation Program of Anhui Province under Project GXXT-2021-028, and the major Project of Zhongshan City, China, under Project 2019AG043. The Associate Editor coordinating the review process was Dr. Sasan Bakhtiari. *(Corresponding author: Gang Wang.)*

Gen Li, Yun Ge, Yiyu Wang, and Gang Wang are with the Department of Electronic Engineering and Information Science, University of Science and Technology of China, Hefei 230027, China (e-mail: gwang01@ustc.edu.cn).

Qingwu Chen is with Zhongshan Erangel Technology Company Ltd., Zhongshan 528437, China.

Digital Object Identifier 10.1109/TIM.2022.3208266

For object detection in NLOS environment, different radars have been adopted with specific NLOS multipath treatment. In the X-band radar detection [1], [2], [3], [4], [5], the multipath echo received by radar is adopted to obtain the micro-Doppler characteristics of moving targets. An algorithm using multipath propagation information of the X-band radar signals to locate static objects behind corners is proposed based on the prior knowledge of the NLOS scene in [6]. In ultrawideband (UWB) radar detections [7], [8], [9], [10], the multipath information derived from the diffraction path and the combined reflection path is used to acquire the two-dimensional positioning of a target in the NLOS region. In [11], the multiple targets localization method using the UWB radar is presented to attain the localization of multiple targets behind the L-shaped corner with complex multipath ghost signals. In [12], multitarget localization in the NLOS region behind an L-shaped corner is acquired by single-channel UWB NLOS target imaging. In [13] and [15], NLOS target detections by using around-the-corner radars are investigated by exploiting the raw signals, including the selection of wall-reflection multipath [14], and the treatment of the corner diffraction and the through-the-wall transmission [15].

Millimeter-wave (mmWave) FMCW radars have also been used to detect hidden targets. In [16], a target location algorithm using the multipath phase difference between multiple channels of a single-input multiple-output mmWave radar is proposed. In [17], synthetic bistatic mmWave radar is used to detect a target behind a corner by exploiting the NLOS multipath returns. In [18], the detection and recognition of the human in the NLOS region by 24-GHz FMCW radar is performed by applying the support vector machine-based machine learning approach to analyze diffraction signals. The 77-GHz FMCW automotive radar is also used to detect and recognize the NLOS moving target by joint NLOS detection and tracking of occluded objects in automotive scenarios [19] and 3-D imaging [20]. For all these NLOS target detections with Doppler radar, UWB radar, and FMCW radar, no vital signs, such as breathing and heart beating, are detected.

For radar-based vital sign detection, quite a lot of works have been reported. Noncontact vital sign monitoring has been conducted with continuous-wave Doppler radar [21], [22], [23], [24], [25], [26], [27], [28], [29], [30], [31]; FMCW radar [32], [33], [34], [35], [36], [37], [38], [39], [40], [41]; and UWB radar [42], [43], [44], [45]. In recent research [39], [40], [41], noncontact vital sign monitoring algorithms utilizing mmWave FMCW radar successfully retrieve respiratory and cardiac information. Although the above detection with

Doppler radar, UWB radar, and FMCW radar may successfully retrieve respiratory and heart rate information, vital sign detection is performed under line-of-sight (LOS) environment. For the NLOS environment, the vital signs could be quite weak and the detection may suffer from strong multipath effects.

To detect a human hidden in the NLOS region, combining NLOS target detection and NLOS vital signs detection can be implemented by using single-channel FMCW radar. Since the human's heartbeat is very weak for radar detection, the breathing of a human is strong enough to be detected by the radar at a relatively long distance, which can be utilized as the most straightforward judgment to discriminate an actionless person from ordinary objects in the NLOS region.

In this article, a single-channel 77-GHz FMCW radar will be used for the on-site detection of actionless humans in the NLOS region. Since the transmitting antenna presents a wide beam (3 dB width of 60°), exact angle information for the radar wave paths cannot be acquired from the raw signal data. In breathing detection with FMCW radar, it is usually required that the accurate position of the hidden person should be provided. An NLOS target positioning algorithm, referred to as the NLOS multipath target searching and position estimating (NLOS-mTSPE) algorithm, is proposed to recognize the typical wave propagation paths in the NLOS region for accurate positioning of the human in the NLOS region. The algorithm is performed by exploiting the on-site raw signals and may acquire accurate human position in the NLOS region.

The article is organized as follows. In Section II, the NLOS electromagnetic (EM) wave reflection and propagation model in an L-shaped corner scene are established for typical NLOS target detection. The NLOS target position estimation algorithm is proposed in Section III by establishing a "path dictionary" according to different "target-radar path" models and looking up the path dictionary for target positioning. In Section IV, breathing rate detection of an actionless person in the NLOS region is demonstrated by two experimental tests. In Section V, the maximum detectable distance and the maximum localizable distance in the NLOS region are analyzed. Section VI concludes this article.

II. Wave Reflection and Propagation Modeling for NLOS Target Detection

Consider an L-shaped corner as shown in Fig. 1, and an mmWave FMCW radar is placed behind the corner and a human is to be detected in the NLOS region. For such a scenario, the Cartesian coordinate system can be defined as in Fig. 1, where the radar is located at the original point O and the target (a person) to be detected is at point $P(x_p, y_p)$. The radar transmits a beam along a direction of azimuth angle θ.

To investigate the NLOS radar detection, the radar wave reflection and propagation models must be established for the L-shaped corner scene in Fig. 1. For the radar signal $s(t)$ transmitted by an antenna at (x_t, y_t), the echo signal received by an antenna at (x_r, y_r) can be expressed, with the bidirectional reflectance distribution function (BRDF) [19], as

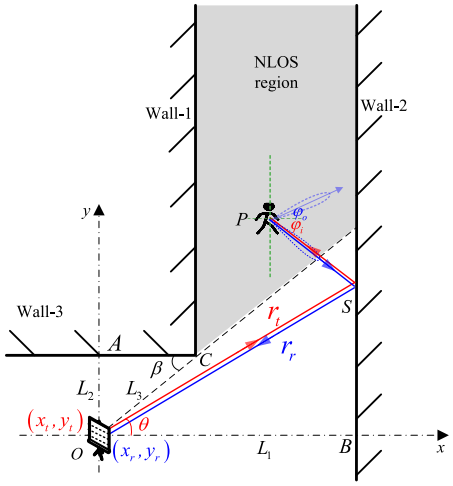

Fig. 1. Detection of a human in the NLOS region behind an L-shaped corner.

$$r(x_t, y_t, x_r, y_r, t) = \iiint_{\Omega} \frac{1}{r_t^2}\frac{1}{r_r^2}\alpha(x, y, z)\rho(\varphi_i, \varphi_o)s\left(t - \frac{r_t + r_r}{c}\right)dxdydz \tag{1}$$

where r_t is the path length of radar wave from the transmitting antenna to the target at P, r_r is the path length of the echoed wave from the target to the receiving antenna, c is the speed of radar wave, $\alpha(x, y, z)$ is the spatially varying albedo on the target surface point (x, y, z), and $\rho(\varphi_i, \varphi_o)$ is the BRDF of radar waves, which is related to the incident direction φ_i and outgoing direction φ_o on the target.

Suppose that the wall will yield specular reflection of EM waves, and the human body will yield specular reflection, retroreflection, and diffuse reflection, as shown in Fig. 1. Since the diffuse reflection is usually quite weak, the retroreflection from the human body makes the key contribution to the radar echo signal [19]. Therefore, we may acquire the range, angle, and Doppler velocity information from the hidden person's retroreflection signal. Such information will be used to estimate the human's position and detect breathing.

In the propagation of radar waves and echoes, diffraction occurs at edge C and specular reflection occurs on the wall. Since the radar waves diffracted from edge C and the waves encountering multiple (thrice or more) reflections are too weak to detect a target, only waves encountering the primary and secondary reflections are to be considered in the radar detection analysis.

Therefore, three types of propagation paths involving primary reflection and secondary reflection are to be included in the NLOS detection model, as shown in Fig. 2. The three paths are given as follows.

1) *Primary Reflection Path:* A round-trip path $O \rightarrow P21 \rightarrow P \rightarrow P21 \rightarrow O$. The transmitted and echoed signals take the same path with one wall reflection.
2) *Secondary Reflection Path:* A round-trip path $O \rightarrow P22 \rightarrow P11 \rightarrow P \rightarrow P11 \rightarrow P22 \rightarrow O$. The radar

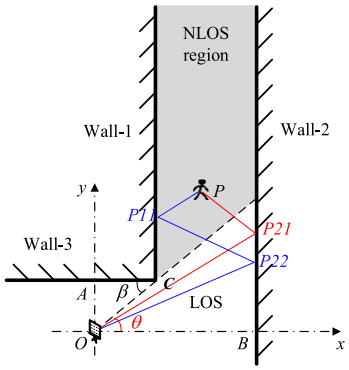

Fig. 2. Typical propagation paths of radar waves in an L-shaped corner region.

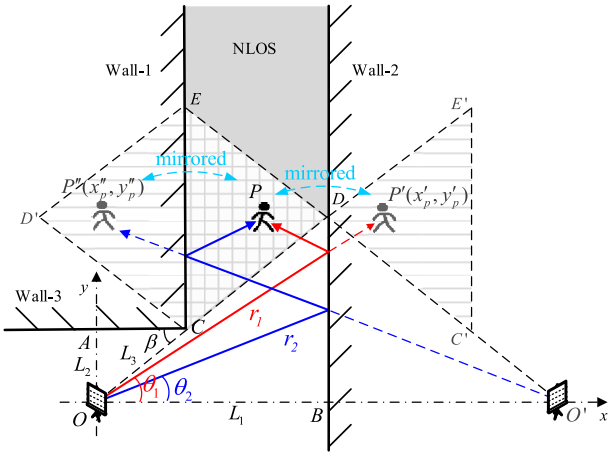

Fig. 3. Path length evaluation for NLOS detection with paths #1 and #2.

wave encounters two wall reflections before impinging onto the person and the echo returns along the same path.

3) *Primary-Secondary Reflection Path:* A combined path $O \rightarrow P21 \rightarrow P \rightarrow P11 \rightarrow P22 \rightarrow O$ or path $O \rightarrow P22 \rightarrow P11 \rightarrow P \rightarrow P21 \rightarrow O$. The transmitted and echoed signals take two different paths, one with two wall reflections and the other with one wall reflection.

III. Target Positioning for NLOS Human Detection

Accurate human position estimation is necessary for accurate breathing detection. Different from the conventional NLOS position estimation methods, we propose a specific on-site target positioning scheme for NLOS detection. First, we survey the L-shaped corner geometry by rotating the mmWave radar. Then, the detection range in the NLOS region can be evaluated, according to the NLOS geometry, by considering the primary and secondary reflection. Finally, the person's position in the NLOS region can be determined by searching among all the possible wave paths defined in Section II.

To ensure that the NLOS environmental geometric parameters and the target (or person) position in the NLOS region can be acquired accurately, the radar system should keep stable during the scanning, the beam should scan horizontally, and the rotation angle should be as fine and accurate as possible. In the following experiment, the radar is set up on a professional tripod with a horizontal scale and a gradienter and rotate the holder with a goniometer as angle indicator.

In practice, a radar antenna has a beamwidth in the azimuth direction. The narrower the beamwidth, the more accurate the position estimation through the radar rotation detection. For radar with a broad beamwidth (such as the one we use in the experiment), the positioning accuracy can be ensured by rotating the radar at a fine angle step, say 2°.

A. Corner Environmental Survey

The L-shaped corner geometry can be characterized by *OA*, *OB*, and *OC* in Fig. 1. The three distances can be measured on-site by rotating the radar system to appropriate angles.

As shown in Fig. 1, EM waves emitted in directions of different azimuth angles have different echoes. When $\theta = 0°$, the distance from the radar antenna to wall-2 can be measured as $\overline{OB} = L_1$. When $\theta = 90°$, the distance from the antenna to wall-3 can be measured as $\overline{OA} = L_2$. Rotating the radar to an appropriate θ that the corner edge is scanned (as indicated in Fig. 3), the distance from the antenna to the wall edge *C* can be measured as $\overline{OC} = L_3$.

With the geometric parameters (L_1, L_2, L_3) of the corner, the radar can be positioned and different wave path lengths for NLOS detection can be evaluated.

B. Target Position Estimation Algorithm

During the scanning of the radar beam for the NLOS region survey, the radar waves reflected from wall-2 will yield an effective survey with the strongest probing energy into the NLOS region.

Since only three types of EM wave paths, i.e., paths #1, #2, and #3 as described in Section II, are involved in NLOS target detection, we may establish a "path dictionary," including all the possible "radar-target-radar path" models. As a result, the positioning of a target in the NLOS region can be implemented by looking up the "path dictionary."

According to the NLOS detection modeling, both the primary reflection path and the secondary reflection path have the minimum–maximum boundaries in the "path dictionary." For the primary reflection path, i.e., path #1, the minimum path length r_{1min} and the maximum path length $r_{1\max}$, as indicated by the red path in Fig. 3, can be calculated by evaluating

$$\begin{aligned} r_{1\min} &= \min \sqrt{x_p'^2 + y_p'^2} \\ r_{1\max} &= \max \sqrt{x_p'^2 + y_p'^2} \\ &\text{s.t. } x_p' < 2L_1 - L_3 \cos\beta \\ &\quad x_p' \tan\beta - y_p' > 0 \\ &\quad x_p' \tan\beta + y_p' - 2L_1 \tan\beta > 0. \end{aligned} \tag{2}$$

For the secondary reflection path, i.e., path #2, the minimum path length r_{2min} and the maximum path length $r_{2\max}$,

as indicated by the blue path in Fig. 3, can be calculated by evaluating

$$\begin{aligned} r_{2min} &= \min \sqrt{\left(x_p'' - 2L_1\right)^2 + y_p''^2} \\ r_{2max} &= \max \sqrt{\left(x_p'' - 2L_1\right)^2 + y_p''^2} \\ &\text{s.t. } x_p'' < L_3 \cos\beta \\ &\quad x_p'' \tan\beta - y_p'' + 2(L_1 \tan\beta - L_2) > 0 \\ &\quad x_p'' \tan\beta + y_p'' - 2L_2 > 0. \end{aligned} \tag{3}$$

The path looking up can thus be restricted within a range as

$$r_{\min} = \min\{r_{1\min}, r_{2\min}\} < r < \max\{r_{1\max}, r_{2\max}\} = r_{\max}. \tag{4}$$

Once the radar wave path (i.e., path #1, #2, or #3) and the path direction and length (i.e., the azimuth angle θ and the path length r) are determined, the target position in the NLOS region can be determined. However, due to the complex static clutters in the NLOS environment, it is hard to directly acquire path length r from the measurement, where the "path dictionary" finds its application.

During the scanning of the radar beam for human detection in the NLOS region, the echoed signal will strengthen if a target is scanned. With the value of the scanning azimuth θ and the length of the path from the radar to the target position, the target position can be determined by looking up the path dictionary.

For the path lookup, we propose an NLOS-mTSPE algorithm. The key idea of the NLOS-mTSPE is to find two or more radar wave paths so that the coordinates of the human position in the NLOS region can be acquired by solving the two path length equations. Solving is implemented by looking up the path direction.

Fig. 4 shows the flowchart of the NLOS-mTSPE algorithm. In the preprocessing stage, FFT is first implemented over the echoed wave data to acquire the range profile. Then, the environmental noise is suppressed partly by using the background subtraction method based on exponential averaging [7]. Finally, a frame of the processed data is selected randomly for processing. The key processing of the NLOS-mTSPE algorithm can be implemented as follows.

Step 1: Initialize the accumulators $A_i = \{a_1, a_2, \ldots, a_M\}$ corresponding to the different ranges. The value of M in our experiment is set as 256, which is defined as the samples per chirp.

Step 2: Traverse the range peaks on different chirps and increase the A_i value corresponding to the peak by one.

Step 3: Set an appropriate threshold s (the maximum value can be the total number of chirps in a frame) and filter out the accumulators f_{Ai}, which are greater than s within the path range ($r_{\min}$, $r_{\max}$).

Step 4: Sort f_{Ai} in descending order of path lengths to sequence the paths for all static targets in a target search range set of $\Psi = \{r_1', r_2', r_3', \ldots\}$.

Step 5: Suppose that $r_1 = r_1'$ is the path length for detection with the primary reflection path, i.e., path #1.

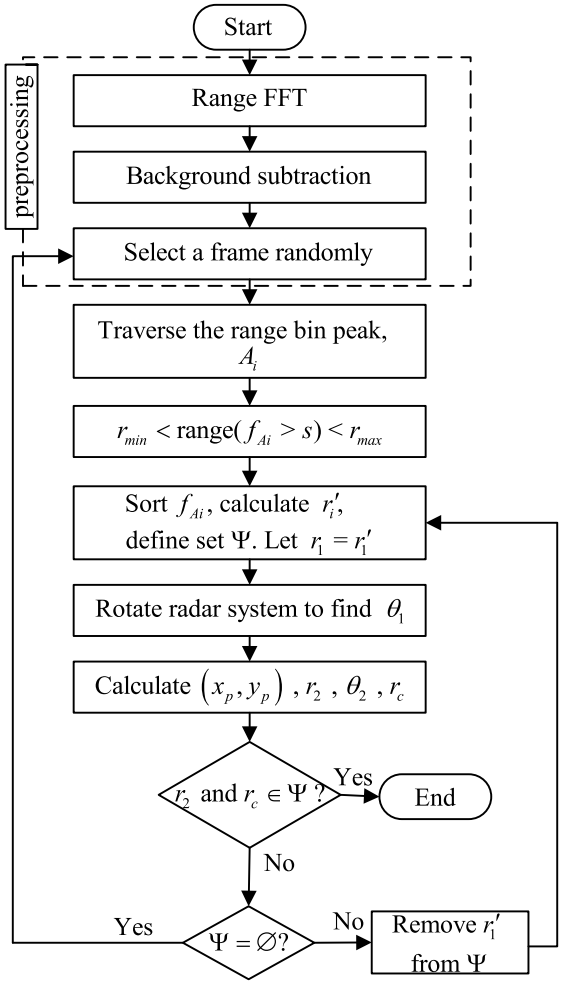

Fig. 4. Processing flow of NLOS-mTSPE algorithm.

Step 6: Perform a horizontal beam scan by rotating the radar at an azimuth angle step of 2°. For each scanning angle θ_{si} ($i = 1, 2, \ldots, n$), record the amplitude values of the echoed wave, which yields $A_{si} = \{a_{s1}, a_{s2}, a_{s3}, \ldots, a_{sn}\}$.

Step 7: Find the azimuth angle θ_1 corresponding to the maximum peak of angle A_{si}.

Step 8: Calculate the target coordinates for detection with the primary reflection, i.e., along path #1, by

$$\begin{cases} x_p = 2L_1 - r_1 \cdot \cos\theta_1 \\ y_p = r_1 \cdot \sin\theta_1. \end{cases} \tag{5}$$

Step 9: Calculate the azimuth θ_2 and the path length r_2 for detection with the secondary reflection, i.e., along path #2, by

$$\begin{cases} r_2 \cos\theta_2 = 2L_1 + x_p - 2L_3 \cos\beta \\ r_2 \sin\theta_2 = y_p. \end{cases} \tag{6}$$

Step 10: Calculate the path length r_c for detection with the combined reflection path, i.e., path #3, as

$$r_c = \frac{r_1 + r_2}{2}. \tag{7}$$

Step 11: Verify whether the calculated r_2 and r_c values belong to set Ψ. If yes, r_1 and the corresponding θ_1 can be

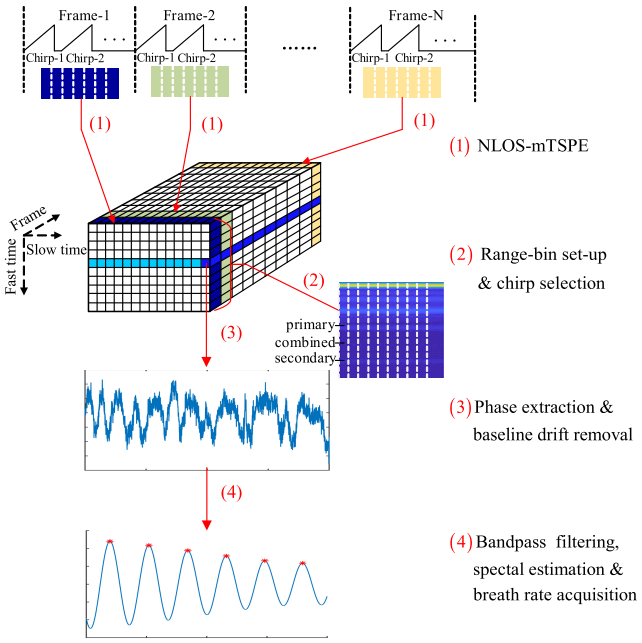

Fig. 5. Schematic for NLOS breathing detection with FMCW radar.

used to position the target as in (5). If no, remove r_1' from set Ψ, update Ψ, and continue the searching from Step 4.

For 20-s radar data segment, the processing time of the NLOS-mTSPE algorithm on MATLAB software takes 1.4291 s on a computer with Intel[1] Core[2] i7-10700 CPU @ 2.90 GHz.

IV. Breathing Detection for NLOS Human Detection

Once a human target can be detected and positioned by using the NLOS-mTSPE algorithm, we may perform the breathing detection. The schematic for breathing detection with FMCW radar is shown in Fig. 5, which includes four key phases.

In phase (1), the NLOS-mTSPE algorithm is utilized to acquire the length of three reflection paths r_1, r_2, and r_c.

In phase (2), the range bins corresponding to each path are set up, and one chirp of them is randomly selected (e.g., the first one in the dark blue cells).

In phase (3), the time-varying phase of the selected chirp corresponding to the continuously varying the frame is extracted and converted into the micro-motion information for the fluctuation of the human chest. The method of removing baseline drift is applied to enhance the breathing signal and remove any other phase drifts.

In phase (4), the phase values are passed through a bandpass filter with a passband between 0.12 and 0.6 Hz, which may filter out the clutter components and yield a continuous stream of the breathing signal. After implementing FFT, the *findpeaks* function in MATLAB software, and peak interval calculation, the clean breathing signals are separated and the breathing rate can be acquired.

[1]Registered
[2]Trademarked

TABLE I
FMCW Radar Parameters for the Experiment

Parameter	Bandwidth	Fs*	Chirp Duration	Samples Per Chirp	Chirps Per Frame
Values	896MHz	20MHz	40us	256	128

*Fs means the sampling frequency in fast time.

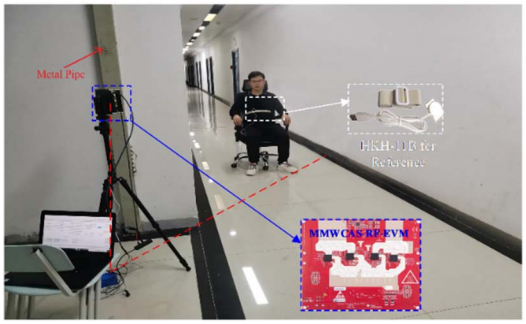

Fig. 6. Experiment setup for NLOS breathing detection with a 77-GHz FMCW radar.

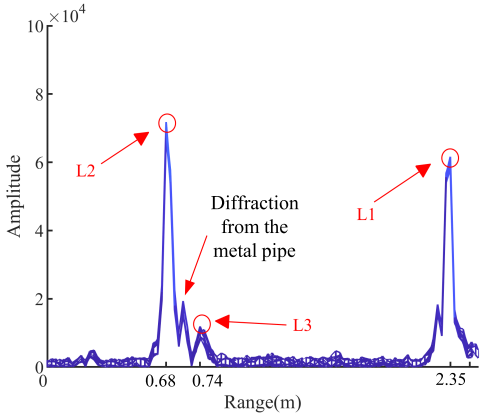

Fig. 7. On-site survey of the corner for geometry measurement.

A. Experiment Setup

The experiment setup for NLOS breathing detection with the *MMWCAS-RF-EVM* 77GHz mmWave FMCW radar is shown in Fig. 6. The radar parameters are listed in Table I. In the detection, we just use one channel of the radar, which provides a radar beamwidth of 60°. The radar system is located on one side of the L-shaped corner, and the person under detection is on the other side of the wall corner. To check the accuracy of radar breathing detection, an HKH-11B commercial respiratory belt sensor is worn by the person to provide the reference breathing rate.

By rotating the radar system to the appropriate azimuth, the environmental geometric parameters (i.e., L_1, L_2, L_3 in Fig. 1) can be readily acquired from the on-site survey data as shown in Fig. 7. In the detection, we scan the radar beam from an initial direction with the radar array faces to wall-3, i.e., from direction with $\theta > 90°$ to $\theta = 0°$ if according to Fig. 1. During the scan, the first peak occurs when $\theta = 90°$

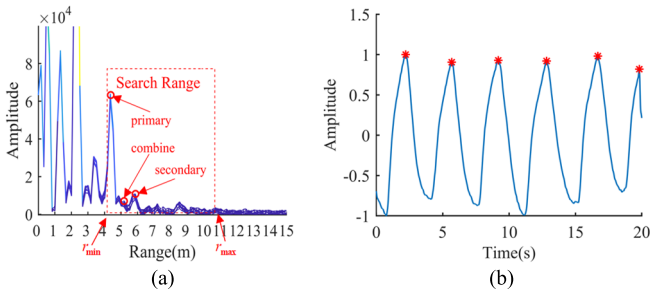

Fig. 8. (a) Radar range FFT data and (b) belt sensor data for the person at position P1 near the wall corner.

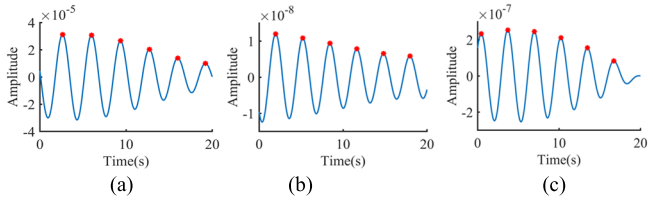

Fig. 9. Breathing signals extracted from the range bins with position P1 corresponding to the lengths of different paths: (a) path #1, (b) path #2, and (c) path #3.

(indicating the peak reflection from wall-3), and thus, L2 is acquired. The second peak occurs when the beam scans the metal pipe. The third peak occurs when the beam scans the corner edge (indicating the corner edge diffraction) and L3 is acquired. The last peak occurs when $\theta = 0°$ (indicating the peak reflection from wall-2) and L1 is acquired. The survey for the L-shaped corner in Fig. 6 yields $L_1 = 2.35$ m, $L_2 = 0.68$ m, and $L_3 = 0.74$ m, which are exactly the same as the real setup. For such an NLOS scenario, the search range in (4) for paths, including the primary and secondary reflections, can be calculated, from (2) and (3), as $r_{\min} = 4.30$ m and $r_{\max} = 10.82$ m for the NLOS-mTSPE.

By rotating the radar to find the target person and positioning with the NLOS-mTSPE algorithm, we can obtain the position information and angle information of the person in the NLOS region. The breathing signal is then extracted from the echoed wave data of the FMCW radar by following the scheme in Fig. 5. For demonstration, we will detect a person at two typical positions in the NLOS region.

B. Breathing Detection of a Person at Different Positions

The first experiment test is carried out with a person in the NLOS region at position P1 near the wall corner C. Fig. 8(a) shows the range FFT of radar echo within the search range of NLOS-mTSPE. Fig. 8(b) shows the real-time breathing signal measured by the HKH-11B commercial respiratory belt sensor. Fig. 9 shows the breathing signals extracted from the range bins corresponding to the lengths of paths #1, #2, and #3 defined in Section II. The breath rate detected by the radar is 18 b/min for path #1, 18 b/min for path #2, and 18 b/min for path #3, which indicates an average breath rate of 18 b/min. The breath rate from the belt sensor is 18 b/min. It can be found that the average breath rate agrees well with the reference value from the belt sensor, with an error less than 1%. Fig. 10 shows the spectra for the belt sensor data and the breathing signals corresponding to paths #1, #2, and #3.

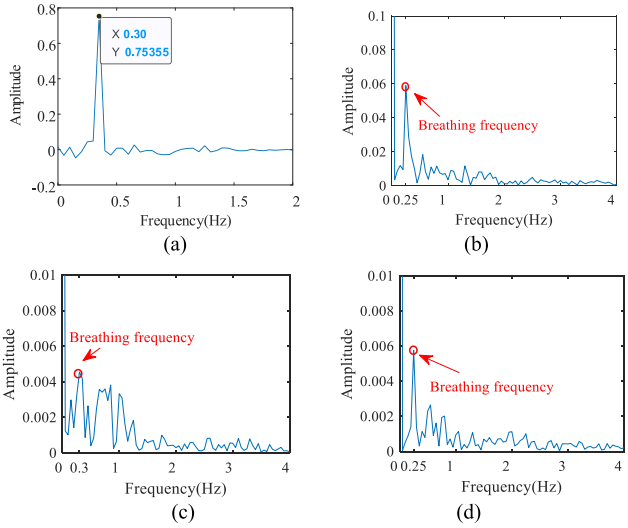

Fig. 10. Spectra for the belt sensor data and the breathing signals for (a) belt sensor data, (b) path #1, (c) path #2, and (d) path #3.

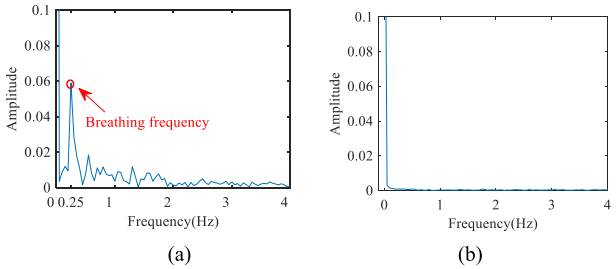

Fig. 11. Spectra of micro-motion signals for path #1 (a) with person in chair and (b) without person in chair.

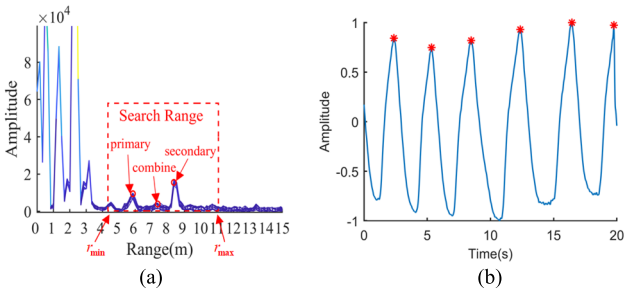

Fig. 12. (a) Radar range FFT data and (b) belt sensor data for the person at position P2 away from the wall corner.

To show the difference between the detection of a chair and a chair with a person sitting in, Fig. 11 shows the spectra of micro-motion signal for path #1 of the chair with and without a person. As shown in Fig. 11(b), no Doppler information can be extracted for the chair without person sitting in.

The second experiment test is carried out with the person at position P2 in the corridor away from the wall corner, which is almost the longest path that can be detected by the radar under the NLOS circumstances. Fig. 12(a) shows

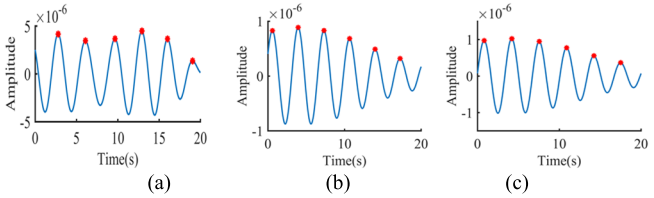

Fig. 13. Breathing signals extracted from the range bins with position P2 corresponding to the lengths of different paths: (a) path #1, (b) path #2, and (c) path #3.

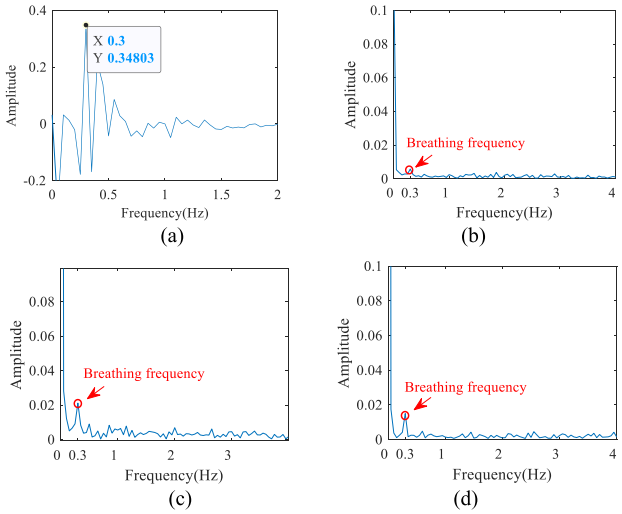

Fig. 14. Spectra for the belt sensor data and the breathing signals for (a) belt sensor data, (b) path #1, (c) path #2, and (d) path #3.

the range FFT of radar echo within the search range of NLOS-mTSPE. Fig. 12(b) shows the real-time breathing signal measured by the HKH-11B commercial respiratory belt sensor. Fig. 13 shows the breathing signals extracted from the range bins corresponding to the lengths of paths #1, #2, and #3. The breath rate detected by the radar is 18 b/min for path #1, 18 b/min for path #2, and 18 b/min for path #3, which indicates an average breath rate of 18 b/min. The breath rate from the belt sensor is 18 b/min. It can be found that the average breath rate agrees well with the reference value from the belt sensor, with an error of less than 1%. Fig. 14 shows the spectra for the belt sensor data and the breathing signals corresponding to paths #1, #2, and #3.

In the two experiment tests, the NLOS-mTSPE algorithm is used to find out the appropriate beam directions of $\theta_1 = 36°$ for the person at P1 and $\theta_1 = 64°$ for the person at P2. Other parameters for the NLOS-mTSPE can be calculated as $\beta = \arcsin(L_2/L_3) = 66°$, $r_{1\min} = 4.30$ m, $r_{1\max} = 10.82$ m, $r_{2\min} = 4.45$ m, $r_{2\max} = 10.82$ m, $r_{\min} = 4.30$ m, and $r_{\max} = 10.82$ m, according to (2)–(4).

Table II lists the estimated lengths of paths #1 and #2, the beam direction of path #2, and the positioning results for the person at P1 and P2. For comparison, the real positions of P1 and P2 are also listed. It is found that the positions of P1 and P2 estimated by the proposed NLOS-mTSPE algorithm agree well with the real positions.

TABLE II
PARAMETERS OF NLOS-mTSPE ALGORITHM

Parameter	r_1	r_2	θ_2	(x_p, y_p)	(x_{real}, y_{real})
P1	4.51m	5.85m	27.5°	(1.05m, 2.65m)	(1.10m, 2.72m)
P2	5.86m	8.37m	39.8°	(2.13m, 5.27m)	(1.96m, 5.18m)

Fig. 15. Detection of two persons in the NLOS region.

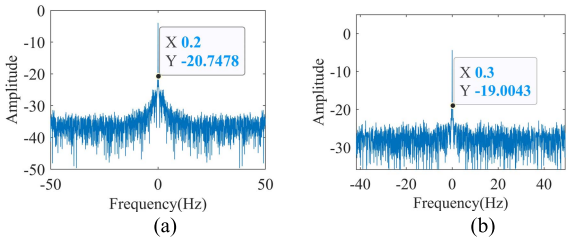

Fig. 16. Spectra of micro-motion signals (a) for person #1 and (b) for person #2.

C. Breathing Detection of Two Persons at Different Positions

An experiment to detect the breathing signals of two people in the NLOS region is conducted, as shown in Fig. 15. The person with black T-shirt stands at 4.52 m away from the radar, and the person with white T-shirt is at 7.36 m away from the radar.

The spectra of extracted micro-motion signals of the two persons are shown in Fig. 16. It is found that the breathing rate of person #1 is 0.2 Hz, while for person #2, it is 0.3 Hz.

V. DETECTION AND LOCATION RANGES IN THE NLOS REGION

For radar detection of a target in an LOS scenario, the radar equation provides the maximum detection range as

$$R_{0\max} = \sqrt[4]{\frac{P_t G_t A_r \sigma}{(4\pi)^2 S_{i\min}}} \tag{8}$$

where P_t is the radar transmitting power, G_t is the gain of the radar antenna, A_r is the effective receiving area of receiving antenna, σ is the scattering cross-sectional area of the target, and $S_{i\min}$ is the minimum detectable signal power of the radar.

For the NLOS detection, the incident EM wave to the target and the echo from the target may take different paths and involve different wall reflections. Suppose that the incident wave has a path length of R_{im} and encountered m wall reflections, and the echo wave has a path length of R_{en} and experienced n wall reflections; the general expression of

maximum detectable distance, as a combination of maximum for R_{im} and R_{en}, can be given as

$$(R_{im}R_{en})_{\max} = \sqrt{\frac{P_t G_t A_r \sigma}{(4\pi)^2 S_{i\min}} \prod_{k=1}^{m+n} \alpha_k(\theta_k)} = R_{0\max}^2 \sqrt{\prod_{k=1}^{m+n} \alpha_k(\theta_k)} \quad (9)$$

where $\alpha_k(\theta_k)$ is the reflection coefficient of the kth wall reflection and θ_k is the incident angle of the kth wall reflection.

With the three types of propagation paths for NLOS detection introduced in Section II, specific detection areas in the NLOS region can be analyzed. Assuming that $\alpha_k(\theta)$ is approximately equal to α, the maximum and minimum path lengths can be acquired by analyzing R_{im}, i.e., for $m = n$ in (9). Therefore, we may discuss the scenarios for detection with the round-trip wave propagation along paths #1 and #2.

For the radar used in the experiment detection in Fig. 6, the maximum detection range of human breathing, i.e., $R_{0\max}$, is approximately 32.00 m in the LOS scenario. The reflection coefficient $\alpha_k(\theta_k)$ of the wall in Fig. 6 can be evaluated as about $\alpha_k(\theta) \approx 0.26$ from (9), according to experimental tests with the FMCW radar detection in front of the same wall in a large hall.

As a result, the maximum path length for NLOS detection with path #1 is approximately $R_{i1\max} \approx 16.32$ m, which can be calculated by (9) with $m = n = 1$. For detection with path #2, the maximum path length can be evaluated as $R_{i2\max} \approx 8.37$ m by setting $m = n = 2$ in (9). For detection with path #3, the maximum path length can be evaluated as $R_{iC\max} \approx 12.35$ m by setting $m = 2$ and $n = 1$ or $m = 1$ and $n = 2$ in (9). The maximum path lengths, together with the radar deployment and the corridor width, will determine the detection and location ranges in the NLOS region.

A. Detectable and Localizable Areas for Detection Within the Maximum Length of Path #1

When the radar is deployed far from wall-3 or the corridor width between wall-1 and -2 is wide enough, path #1 yields the longest path length.

For detection with path #1, the detectable area in the NLOS region will be restricted by the longest path length $R_{i1\max}$, as indicated by the area *CDRQC* in Fig. 17. The arc RQ has a radius of $R_{i1\max}$ centered at O', which is the mirror-symmetrical point of the radar about wall-2.

When the target is within the detectable area *CDRQC*, detection with path #2 or #3 may occur as well. If the detection with path #2 and/or #3 can be measured, as in the case shown in Figs. 8(a) and 12(a), a different detection path (e.g., along path #2) can link the radar and the target. The two paths characterized by (θ_1, R_{i1}) and (θ_2, R_{i2}) will fix the position of the human target. Thus, path #2 or #3 can be viewed as the location path.

For the location path of maximum length $R_{i2\max}$, the location area can be defined by *CMPNC*. The arc *MPN* has a radius of $R_{i2\max}$ centered at O'', which is the secondary mirror-symmetrical point of radar about wall-2 and -1, as shown in Fig. 17.

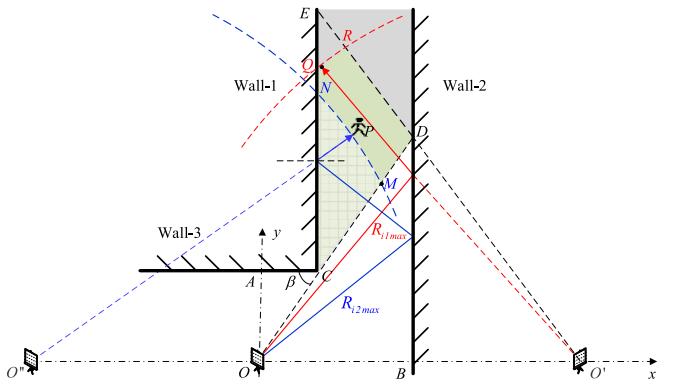

Fig. 17. Detectable and localizable areas for NLOS detection within the maximum length of path #1.

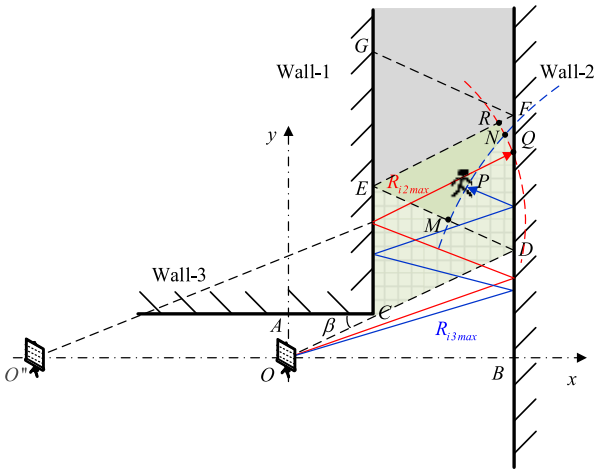

Fig. 18. Detectable and localizable areas for NLOS detection when high-order paths (path #2 and path with triple wall reflections) are involved.

Therefore, the breathing of a human target can be detected in the detectable area *CDRQC*, while the human target can be accurately positioned in the location area *CMPNC*, which is characterized by

$$\begin{cases} x_p > L_3 \cos\beta \\ x_p \tan\beta - y_p < 0 \\ \left[x_p - 2(L_3\cos\beta - L_1)\right]^2 + y_p^2 \le R_{i2\max}^2. \end{cases} \quad (10)$$

For the experiment scenario shown in Fig. 6, the maximum detectable distance between the target and the radar in the y-axis direction is $y_R = \min\{R_{i1\max} \cdot \sin\beta, |\overline{O'E}| \cdot \sin\beta\} = 9.88$ m, while the maximum localizable distance is 8.37 m.

B. Detectable and Localizable Areas for Detection With High-Order Paths Involved

When the radar is properly deployed in front of wall-3 and the corridor width is not so wide, $R_{i2\max} > \overline{OCDE}$ so that a human target in the area outside triangle *CDE* in the corridor,

as shown in Fig. 18, can be detected by wave propagation along path #2.

For the detection with path #2, the detectable area in the NLOS region will be restricted by the longest path length $R_{i2\max}$, as indicated by the area *CDQNREC* in Fig. 18. The arc QNR has a radius of $R_{i2\max}$ centered at O''.

When the target is within the detectable area *CDQNREC*, detection with a high-order path (e.g., including 3 wall reflections and a maximum path length $R_{i3\max}$) may occur and serve as the location path. The location area for the high-order reflection path can be defined by *CDQNPMEC*, where the arc NPM has a radius of $R_{i3\max}$ centered at O''', which is the third mirror-symmetrical point of radar about wall-2, -1, and -2, as shown in Fig. 18.

In this case, the breathing of a human target can be detected in the detectable area *CDQNREC*, while the human target can be accurately positioned in the location area *CDQNPMEC*, which is characterized by

$$\begin{cases} x_p > L_3 \cos\beta \\ x_p \tan\beta - y_p < 0 \\ \left(x_p - 2L_1\right)\tan\beta + y_p < 0 \end{cases} \tag{11}$$

and

$$\begin{cases} \left(x_p - 2L_1\right)\tan\beta + y_p > 0 \\ x_p < L_1 \\ \left[x_p - 2(L_3\cos\beta - L_1)\right]^2 + y_p^2 \le R_{i2\max}^2 \\ \left[x_p - 2(2L_1 - L_3\cos\beta)\right]^2 + y_p^2 \le R_{i3\max}^2. \end{cases} \tag{12}$$

For the experiment scenario shown in Fig. 6, the maximum detectable distance between the target and the radar in the y-axis direction is $y_R = \min\{R_{i2\max}\cdot\sin\beta, |\overline{O''F}|\cdot\sin\beta\} = 7.65$ m.

We remark here that, for a too wide corridor where the round-trip distance between wall-1 and wall-2 is larger than $R_{i1\max}$, the NLOS detection may fail to work. One solution to this issue is to increase the transmitting power or the gain of FMCW radar. For the *MMWCAS-RF-EVM* 77-GHz mmWave FMCW radar, multichannel or array operation may help.

C. Influence of Range and Phase Estimation Errors on Positioning

Reliable target location estimation depends on high accuracy estimation of path range r_1 and phase θ_1. In case there is no error in the estimation, the target coordinates can be acquired by (5). However, the limited bandwidth of radar will have a range resolution so that the estimation of r_1 usually has an error Δr_1 and θ_1 has $\Delta\theta_1$. As a result, ambiguity will be occurring in the positioning result, as indicated by the shadow area *GHNM* in Fig. 19.

Suppose that the mirror target point P' has coordinates (x'_p, y'_p) and the estimated target point M has coordinates (x_M, y_M), and the error of the target position estimation due to range resolution can be calculated by

$$\begin{cases} \Delta x = \left|x_M - x_{p'}\right| = \left|(r_1 + \Delta r_1)\cos(\theta_1 + \Delta\theta_1) - r_1\cos\theta_1\right| \\ \Delta y = \left|y_M - y_{p'}\right| = \left|(r_1 + \Delta r_1)\sin(\theta_1 + \Delta\theta_1) - r_1\cdot\sin\theta_1\right|. \end{cases} \tag{13}$$

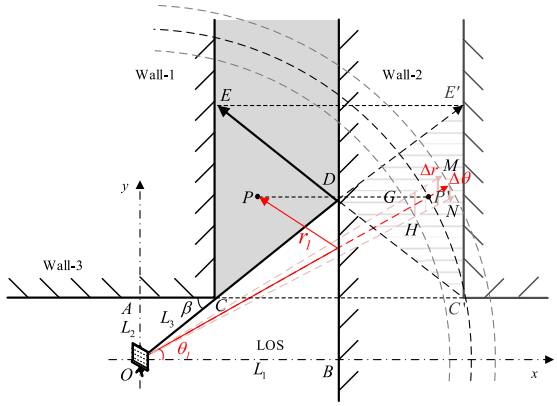

Fig. 19. Influence of r_1 and θ_1 error of the target position estimation.

TABLE III
COMPARISON WITH STATE-OF-THE-ART WORKS

Refs.	Radar	Targets	Strategy / Method
This work	77GHz FMCW single channel	Actionless human (NLOS)	‣ Positioning and vital sign detection ‣ NLOS-mTSPE
[19]	77GHz FMCW MIMO	Pedestrians and cyclists (NLOS).	‣ Detection and tracking ‣ Collision warning
[20]	77GHz FMCW MIMO	Objects (NLOS)	LAC modeling 3-D imaging algorithm.
[33]	5.8GHz FMCW antenna rotation	Indoor human (LOS)	‣ Clutters removal ‣ Location mapping ‣ Vital sign/ gesture
[36]	5.8GHz FMCW slide rail platform	Human (LOS)	‣ 2-D SAR imaging ‣ Human identification
[38]	24GHz FMCW	Human (LOS)	‣ RSMs removal ‣ Vital sign
[41]	77GHz FMCW Single channel	Human (LOS)	‣ Improved MCA algorithm ‣ APVMD algorithm

The errors in range and phase estimation will affect the breath detection as well. According to (5) and (6), the errors Δr_1 and $\Delta\theta_1$ will yield errors Δr_2 and $\Delta\theta_2$ in r_2 and θ_2, respectively. Once the length estimation error exceeds half of the range resolution of the radar, the range FFT peak will have an ambiguity. For the radar parameters in Table I, the range resolution of the mmWave FMCW radar can be calculated as

$$d_{\text{res}} = \frac{c}{2B} = 0.167 \text{ m} \tag{14}$$

where c is the speed of EM wave and B is the sweep bandwidth. If $\Delta r_1 < d_{\text{res}}/2 = 0.0835$ m and $\Delta r_2 < d_{\text{res}}/2 = 0.0835$ m, the peak value of the range FFT corresponding to path length r_1 and r_2 may keep unchanged. As a result, the proposed NLOS-mTSPE algorithm can do positioning accurate enough, and the breathing signals can be extracted for all the three paths #1, #2, and #3; otherwise, the proposed NLOS-mTSPE algorithm may fail to position.

VI. Conclusion

Detection of human breathing in the NLOS region may benefit the recognition of hidden or actionless human. This article mainly studies target position estimation and breathing signal extraction by utilizing mmWave FMCW radar under NLOS conditions. The positioning method can accurately estimate the target position by judging the length of different reflection paths. Moreover, the breathing signal can be extracted by further analyzing the radar echo. A comparison with other similar state-of-the-art works is shown in Table III.

The NLOS detection and positioning in this article are demonstrated by using a single-channel FMCW radar in a relatively simple scenario of an L-shaped corner. In the future work, we will consider a more complex multipath environment with the interference of strong scattering from multiple targets. Full channel operation of the FMCW radar, and multiple-input–multiple-output (MIMO) radar, will be considered to enlarge the detection range in the NLOS region and to improve the accuracy of the position estimation algorithm.

References

[1] R. Linnehan and J. Schindler, "Validating multipath responses of moving targets through urban environments," in *Proc. IEEE Radar Conf.*, Arlington, VA, USA, May 2010, pp. 1036–1041.

[2] A. Sume *et al.*, "Radar detection of moving targets behind corners," *IEEE Trans. Geosci. Remote Sens.*, vol. 49, no. 6, pp. 2259–2267, Jun. 2011.

[3] M. Gustafsson, A. Andersson, T. Johansson, S. Nilsson, A. Sume, and A. Orbom, "Extraction of human micro-Doppler signature in an urban environment using a 'sensing-behind-the-corne' radar," *IEEE Geosci. Remote Sens. Lett.*, vol. 13, no. 2, pp. 187–191, Feb. 2016.

[4] T. Johansson, Å. Andersson, M. Gustafsson, and S. Nilsson, "Positioning of moving non-line-of-sight targets behind a corner," in *Proc. Eur. Radar Conf.*, London, U.K., 2016, pp. 181–184.

[5] M. Gustavsson *et al.*, "Micro-Doppler extraction of a small UAV in a non-line-of-sight urban scenario," *Proc. SPIE*, vol. 10188, May 2017, Art. no. 101880U.

[6] M. Gustafsson, "Positioning of objects behind corners using X-band radar," in *Proc. 30th URSI Gen. Assem. Sci. Symp.*, Istanbul, Turkey, Aug. 2011, pp. 1–4.

[7] R. Zetik, M. Eschrich, S. Jovanoska, and R. S. Thoma, "Looking behind a corner using multipath-exploiting UWB radar," *IEEE Trans. Aerosp. Electron. Syst.*, vol. 51, no. 3, pp. 1916–1926, Jul. 2015.

[8] S. Li *et al.*, "NLOS target localization with a UWB radar," in *Proc. IEEE Radar Conf. (RadarConf)*, Boston, MA, USA, Apr. 2019, pp. 1–5.

[9] S. Fan *et al.*, "Moving target localization behind L-shaped corner with a UWB radar," in *Proc. IEEE Radar Conf.*, Boston, MA, USA, Aug. 2019, pp. 1–5.

[10] X. Yang, S. Fan, S. Guo, S. Li, G. Cui, and W. Zhang, "NLOS target localization behind an L-shaped corner with an L-band UWB radar," *IEEE Access*, vol. 8, pp. 31270–31286, 2020.

[11] S. Li *et al.*, "Multiple targets localization behind L-shaped corner via UWB radar," *IEEE Trans. Veh. Technol.*, vol. 70, no. 4, pp. 3087–3100, Apr. 2021.

[12] Q. Tang, J. Li, L. Wang, Y. Jia, and G. Cui, "Multipath imaging for NLOS targets behind an L-shaped corner with single-channel UWB radar," *IEEE Sensors J.*, vol. 22, no. 2, pp. 1531–1540, Jan. 2022.

[13] K.-P.-H. Thai *et al.*, "Around-the-corner radar: Detection and localization of a target in non-line of sight," in *Proc. IEEE Radar Conf. (RadarConf)*, Seattle, WA, USA, May 2017, pp. 842–847.

[14] K.-P.-H. Thai *et al.*, "Detection–Localization algorithms in the around-the-corner radar problem," *IEEE Trans. Aerosp. Electron. Syst.*, vol. 55, no. 6, pp. 2658–2673, Dec. 2019.

[15] S. Vishwakarma, A. Rafiq, and S. S. Ram, "Micro-Doppler signatures of dynamic humans from around the corner radar," in *Proc. IEEE Int. Radar Conf. (RADAR)*, Florence, Italy, Apr. 2020, pp. 169–174.

[16] S. Guo, Q. Zhao, G. Cui, S. Li, L. Kong, and X. Yang, "Behind corner targets location using small aperture millimeter wave radar in NLOS urban environment," *IEEE J. Sel. Topics Appl. Earth Observ. Remote Sens.*, vol. 13, pp. 460–470, 2020.

[17] H. Du, C. Fan, C. Cao, Z. Xu, and X. Huang, "A novel NLOS target localization method with a synthetic bistatic MMW radar," in *Proc. IEEE 11th Sensor Array Multichannel Signal Process. Workshop*, Jun. 2020, pp. 1–5.

[18] J. He, S. Terashima, H. Yamada, and S. Kidera, "Diffraction signal-based human recognition in non-line-of-sight (NLOS) situation for millimeter wave radar," *IEEE J. Sel. Topics Appl. Earth Observ. Remote Sens.*, vol. 14, pp. 4370–4380, 2021.

[19] N. Scheiner *et al.*, "Seeing around street corners: Non-line-of-sight detection and tracking in-the-wild using Doppler radar," in *Proc. IEEE/CVF Conf. Comput. Vis. Pattern Recognit. (CVPR)*, Seattle, WA, USA, Jun. 2020, pp. 2065–2074.

[20] S. Wei *et al.*, "Nonline-of-sight 3-D imaging using millimeter-wave radar," *IEEE Trans. Geosci. Remote Sens.*, vol. 60, pp. 1–18, 2022.

[21] A. D. Droitcour, O. Boric-Lubecke, V. M. Lubecke, J. Lin, and G. T. A. Kovacs, "Range correlation and I/Q performance benefits in single-chip silicon Doppler radars for noncontact cardiopulmonary monitoring," *IEEE Trans. Microw. Theory Techn.*, vol. 52, no. 3, pp. 838–848, Mar. 2004.

[22] C. Li, J. Ling, J. Li, and J. Lin, "Accurate Doppler radar noncontact vital sign detection using the RELAX algorithm," *IEEE Trans. Instrum. Meas.*, vol. 59, no. 3, pp. 687–695, Mar. 2010.

[23] C. Gu, C. Li, J. Lin, J. Long, J. Huangfu, and L. Ran, "Instrument-based noncontact Doppler radar vital sign detection system using heterodyne digital quadrature demodulation architecture," *IEEE Trans. Instrum. Meas.*, vol. 59, no. 6, pp. 1580–1588, Jun. 2010.

[24] J. Wang, X. Wang, L. Chen, J. Huangfu, C. Li, and L. Ran, "Noncontact distance and amplitude-independent vibration measurement based on an extended DACM algorithm," *IEEE Trans. Instrum. Meas.*, vol. 63, no. 1, pp. 145–153, Jan. 2014.

[25] Y. S. Lee, P. N. Pathirana, C. L. Steinfort, and T. Caelli, "Monitoring and analysis of respiratory patterns using microwave Doppler radar," *IEEE J. Transl. Eng. Health Med.*, vol. 2, pp. 1–12, 2014.

[26] J. Tu and J. Lin, "Fast acquisition of heart rate in noncontact vital sign Radar measurement using time-window-variation technique," *IEEE Trans. Instrum. Meas.*, vol. 65, no. 1, pp. 112–122, Jan. 2016.

[27] Q. Lv *et al.*, "Doppler vital signs detection in the presence of large-scale random body movements," *IEEE Trans. Microw. Theory Techn.*, vol. 66, no. 9, pp. 4261–4270, Sep. 2018.

[28] D. Tang, J. Wang, W. Hu, Z. Peng, Y.-C. Chiang, and C. Li, "A DC-coupled high dynamic range biomedical radar sensor with fast-settling analog DC offset cancelation," *IEEE Trans. Instrum. Meas.*, vol. 68, no. 5, pp. 1441–1450, May 2019.

[29] J. Saluja, J. Casanova, and J. Lin, "A supervised machine learning algorithm for heart-rate detection using Doppler motion-sensing radar," *IEEE J. Electromagn., RF Microw. Med. Biol.*, vol. 4, no. 1, pp. 45–51, Mar. 2020.

[30] W. Xia, Y. Li, and S. Dong, "Radar-based high-accuracy cardiac activity sensing," *IEEE Trans. Instrum. Meas.*, vol. 70, pp. 1–13, 2021.

[31] J. Y. Shih and F. K. Wang, "Quadrature cosine transform (QCT) with varying window length (VWL) technique for noncontact vital sign monitoring using a continuous-wave (CW) radar," *IEEE Trans. Microw. Theory Techn.*, vol. 70, no. 3, pp. 1639–1650, Mar. 2022.

[32] G. Wang, J.-M. Muñoz-Ferreras, C. Gu, C. Li, and R. Gómez-García, "Application of linear-frequency-modulated continuous-wave (LFMCW) radars for tracking of vital signs," *IEEE Trans. Microw. Theory Techn.*, vol. 62, no. 6, pp. 1387–1399, Jun. 2014.

[33] G. Wang, C. Gu, T. Inoue, and C. Li, "A hybrid FMCW-interferometry radar for indoor precise positioning and versatile life activity monitoring," *IEEE Trans. Microw. Theory Techn.*, vol. 62, no. 11, pp. 2812–2822, Nov. 2014.

[34] Z. Peng *et al.*, "A portable FMCW interferometry radar with programmable low-IF architecture for localization, ISAR imaging, and vital sign tracking," *IEEE Trans. Microw. Theory Techn.*, vol. 65, no. 4, pp. 1334–1344, Apr. 2017.

[35] W. Chen, S. Daneau, C. Brosseau, and F. Heide, "Steady-state non-line-of-sight imaging," in *Proc. IEEE/CVF Conf. Comput. Vis. Pattern Recognit. (CVPR)*, Long Beach, CA, USA, Jun. 2019, pp. 6783–6792.

[36] J. Yan, G. Zhang, H. Hong, H. Chu, C. Li, and X. Zhu, "Phase-based human target 2-D identification with a mobile FMCW radar platform," *IEEE Trans. Microw. Theory Techn.*, vol. 67, no. 12, pp. 5348–5359, Dec. 2019.

[37] K. Liu, C. Ding, and Y. Zhang, "A Coarse-to-Fine robust estimation of FMCW radar signal for vital sign detection," in *Proc. IEEE Radar Conf. (RadarConf)*, Florence, Italy, Sep. 2020, pp. 1–6.
[38] E. Cardillo, C. Li, and A. Caddemi, "Vital sign detection and radar self-motion cancellation through clutter identification," *IEEE Trans. Microw. Theory Techn.*, vol. 69, no. 3, pp. 1932–1942, Mar. 2021.
[39] W. Chen, S. Lan, and G. Zhang, "Multiple-target vital signs sensing using 77 GHz FMCW radar," in *Proc. 15th Eur. Conf. Antennas Propag. (EuCAP)*, Mar. 2021, pp. 1–3.
[40] Q. Wu, Z. Mei, Z. Lai, D. Li, and D. Zhao, "A non-contact vital signs detection in a multi-channel 77 GHz LFMCW radar system," *IEEE Access*, vol. 9, pp. 49614–49628, 2021.
[41] X. Zhang, Z. Liu, Y. Kong, and C. Li, "Mutual interference suppression using signal separation and adaptive mode decomposition in noncontact vital sign measurements," *IEEE Trans. Instrum. Meas.*, vol. 71, pp. 1–15, 2022.
[42] L. Qiu, T. Jin, B. Lu, and Z. Zhou, "An isophase-based life signal extraction in through-the-wall radar," *IEEE Geosci. Remote Sens. Lett.*, vol. 14, no. 2, pp. 193–197, Feb. 2017.
[43] K. Wang, Z. Zeng, and J. Sun, "Through-wall detection of the moving paths and vital signs of human beings," *IEEE Geosci. Remote Sens. Lett.*, vol. 16, no. 5, pp. 717–721, May 2019.
[44] K.-K. Shyu, L.-J. Chiu, P.-L. Lee, T.-H. Tung, and S.-H. Yang, "Detection of breathing and heart rates in UWB radar sensor data using FVPIEF-based two-layer EEMD," *IEEE Sensors J.*, vol. 19, no. 2, pp. 774–784, Jan. 2019.
[45] X. Shang, J. Liu, and J. Li, "Multiple object localization and vital sign monitoring using IR-UWB MIMO radar," *IEEE Trans. Aerosp. Electron. Syst.*, vol. 56, no. 6, pp. 4437–4450, Dec. 2020.

Gen Li was born in China, in 1994. He received the B.S. degree in electronic and information engineering from the Anhui University of Finance and Economics, Bengbu, China, in 2018. He is currently pursuing the Ph.D. degree in communication and information engineering with the School of Information Science and Technology, University of Science and Technology of China, Hefei, China.

His research interests are in radar signal processing and bioradar design. He is researching radar vital sign detection.

Yun Ge was born in China, in 1997. She received the B.S. degree in electronic information engineering from the School of Electronic Engineering and Optoelectronic Technology, Nanjing University of Science and Technology, Nanjing, China, in 2019. She is currently pursuing the Ph.D. degree with the School of Information Science and Technology, University of Science and Technology of China, Hefei, China.

Her research interests are in data-driven-based radar signal processing. She is researching dynamic posture recognition for humans in NLOS.

Yiyu Wang was born in China, in 1999. He received the B.S. degree in electronic information science and technology from the School of Physics and Optoelectronic Engineering, Xidian University, Xi'an, China, in 2020. He is currently pursuing the Ph.D. degree with the School of Information Science and Technology, University of Science and Technology of China, Hefei, China.

His research interests are in radar signal processing. He is researching bioradar signal processing and human recognition.

Qingwu Chen was born in China, in 1967. He received the B.S. degree from the Department of Radio Electronics (now the Department of Electronic Engineering and Information Science), University of Science and Technology of China, Hefei, China, in 1983, and the M.S. degree in biomedical engineering from Sun Yat-sen University, Guangzhou, China, in 1991.

He is currently the CEO of Zhongshan Erangel Technology Company Ltd., Zhongshan, China.

Gang Wang (Member, IEEE) received the B.S. degree from the University of Science and Technology of China, Hefei, China, in 1988, and the M.S. and Ph.D. degrees in electrical engineering from Xidian University, Xi'an, China, in 1991 and 1996, respectively.

From 1996 to 1998, he was a Post-Doctoral Research Fellow, supported by the Chinese Government, with Xi'an Jiaotong University, Xi'an, where he was an Associate Professor from 1998 to 2000. In 2001, he joined the Department of ITM, Mid-Sweden University, as a Visiting Researcher. From 2002 to 2003, he was a Post-Doctoral Research Associate with the Department of Electrical and Computer Engineering, University of Florida, Gainesville, FL, USA. From 2003 to 2010, he was a Chair Professor with Jiangsu University, Zhenjiang, China. He is currently a Full Professor with the University of Science and Technology of China. His current research interests include bioradar signal processing, autonomous driving, radio frequency identification (RFID)/sensor technology, and microwave circuit and antenna design.